RSC Advances

PAPER

View Article Online
View Journal | View Issue

Cite this: *RSC Adv.*, 2022, **12**, 24769

Dual-ZIF-derived "reassembling strategy" to hollow MnCoS nanospheres for aqueous asymmetric supercapacitors†

Song Liu,[a] Kun Chen,[a] Changguo Xue, *[a] Shibin Nie,*[bc] Jianjun Li [a] and Jinbo Zhu[a]

Construction of delicate nanostructures with a facile, mild-condition and economical method is a key issue for building high-performance electrode materials. We demonstrate a facile and novel "reassembling strategy" to hollow MnCoS nanospheres derived from dual-ZIF for supercapacitors. The spherical shell's surface structure, thickness and Mn distribution were controlled by regulating the solvothermal reaction time. The chemical composition, phases, specific surface areas and microstructure were studied and the electrochemical performances were systematically estimated. As the unique low-crystalline and optimized hollow nanosphere structure contributes to increasing active sites, MnCoS nanospheres exhibit excellent electrochemical performance. The test results show that the specific capacitance increases with increasing solvothermal time, and the MCS with a 5 h reaction time exhibits optimal electrochemical properties with a high specific capacity of 957 C g^{-1} (1 A g^{-1}). Furthermore, an MCS-5//AC asymmetric supercapacitor device delivers a specific energy as high as 36.9 W h kg^{-1} at a specific power of 750 W kg^{-1}.

Received 25th June 2022
Accepted 24th August 2022

DOI: 10.1039/d2ra03914a

rsc.li/rsc-advances

Introduction

To solve the current energy crisis and serious environmental problems, novel electrochemical energy storage equipment with high efficiency has been considered as one of the solutions.[1,2] Among the numerous energy storage devices, supercapacitors deliver high power density, have a fast charge–discharge process and long cycling life, and are widely used in military equipment, intelligent instruments and hybrid vehicles.[3,4] For practical uses, asymmetric supercapacitors (ASCs) were fabricated by employing the battery type electrode and electric double-layer electrode in one cell. Nevertheless, the low energy density limits the further development of supercapacitors.[5–7] The battery-type electrode can cause redox reactions which is a crucial component to improve electrochemical performance, and the current research focuses on the effective synthesis of high-capacity electrode materials.

In recent years, the transition metallic sulfide as electrode material has attracted tremendous attention due to its high electronic conductivity and capacitance.[5,8,9] In particular, the manganese cobalt sulfides (MCS) have advantages such as rich reaction sites, bimetallic synergistic effects and multiple redox electrical pairs of Mn and Co ions, which strongly proves excellent electrochemical performance in supercapacitors. Wie *et al.* designed hierarchical $MnCo_2S_4$ nanotubes, displaying a large capacitance of 705.2 F g^{-1} (0.5 A g^{-1}).[10] Elshahawy *et al.* reported controllable $MnCo_2S_4$ nanostructures displaying large capacitance of 1402 F g^{-1} (1 A g^{-1}) and long-term cycling reliability (95% retention after 5000 cycles).[11]

Nanostructure and morphology controlling is another efficient way to boost the properties of electrodes.[12–14] Various manganese cobalt sulfide nanostructures have been designed and fabricated with excellent performances (nanoparticles,[15] nanoplates,[16] hollow and porous nanostructure[10]). Among them, hierarchical hollow structure composed of small nanoparticles can improve the electrochemical performance due to interior voids increasing the interface infiltration, active sites and ion diffusion paths. Shen *et al.* synthesized uniform nickel cobalt glycerate solid spheres precursor and transformed the solid spheres into nickel cobalt sulfide hollow spheres, revealing a high specific capacitance of 1036 F g^{-1} (1 A g^{-1}).[17] Peng prepared CoS_2 solid microspheres and transformed them into a hollow structure *via* a solution-based method. The resulting hollow CoS_2 spheres demonstrate excellent supercapacitive performance.[18] In general, reasonable construction and controllable synthesis of the suitable templates are the critical processes for the delicate hollow structures.[19]

[a]*School of Materials Science and Engineering, Anhui University of Science and Technology, Huainan, Anhui 232001, P. R. China. E-mail: chgxue@aust.edu.cn; nsb@mail.ustc.edu.cn*

[b]*School of Safety Science and Engineering, Anhui University of Science and Technology, Huainan, Anhui 232001, P. R. China*

[c]*Institute of Energy, Hefei Comprehensive National Science Center (Anhui Energy Laboratory), Hefei, Anhui 230000, P. R. China*

† Electronic supplementary information (ESI) available. See https://doi.org/10.1039/d2ra03914a

Zeolitic imidazolate frameworks (ZIFs), with the advantages of regulable morphology, composition and functional diversity, have been utilized as an ideal template for synthesizing nanostructures.[20–22] Diversity of ZIFs and its derivatives with fine nanostructure such as $NiCo_{2-x}Fe_xO_4$ nano boxes,[23] Co_9S_8 nanoparticles,[24] double-shell ZnCoS dodecahedrons,[25] were synthesized and utilized in the fields of electrochemical catalysis, battery and supercapacitor. Tang *et al.* reported mesoporous carbon composite with core–shell structure derived from dual-ZIF (ZIF8@ZIF-67), displaying superior capacitance of 270 F g^{-1} (1 A g^{-1}).[26] Pan *et al.* synthesized $NiFe_2O_4$/$NiCo_2O_4$/GO composites *via* pyrolysis method derived from dual MOF (FeNi-MIL-88/NiCo-MOF-74), revealing a high specific capacitance of 661 C g^{-1} (1 A g^{-1}) and excellent cycling stability with 89.9% retention after 3000 cycles.[27] Whereas most dual-ZIF assemble processes were restricted by the lattice incompatibility, a high consumption calcination method was needed. The fabrication of manganese cobalt sulfide with a facile, mild-condition and economical routine remains a significant challenge.

In this work, a novel hollow manganese cobalt sulfides nanospheres was synthesized using a dual-ZIF-derived "reassemble strategy" from Co-ZIF and Mn-ZIF. The spherical shell surface structure, thickness and chemical composition, especially the Mn-ion sites, were controlled *via* regulating the solvothermal reaction time. As the optimized hollow nanosphere structures contribute to increasing active sites, MCS exhibited excellent electrochemical properties. The results showed that the specific capacitance increases with increasing solvothermal time, and the MCS with 5 h reacting time exhibited optimal electrochemical properties with the highest specific capacity of 957 C g^{-1} (1 A g^{-1}). Furthermore, an MCS-5//AC asymmetric supercapacitor device delivers an energy density as high as 36.9 W h kg^{-1} at a power density of 750 W kg^{-1}.

Experimental

Synthesis of Mn, Co-ZIF precursor

All chemicals and solvents were of analytical grade and used without purification. In order to synthesize Mn, Co-ZIF precursor, 1 mmol $CoCl_2 \cdot 6H_2O$ and 0.5 mmol $MnCl_2 \cdot 4H_2O$ were dissolved in 3 mL deionized (DI) water. 5.5 g 2-methylimidazole (2-MIM) was dissolved in 20 mL DI water. After stirring for 10 min, the two solutions were rapidly mixed and stirred thoroughly at room temperature for 10 h. The resulting product was centrifuged and washed with DI water and ethanol. Then, the purple powder was dried overnight in an oven at 60 °C. Moreover, Co-ZIF or Mn-ZIF precursor can be obtained with the same procedure by adding only 1.5 mmol $CoCl_2 \cdot 6H_2O$ or 1.5 mmol $MnCl_2 \cdot 4H_2O$.

Synthesis of manganese cobalt sulfide

80 mg of the MnCo-ZIF precursor was dispersed into 25 mL ethanol through ultrasound treatment. Afterwards, 120 mg thioacetamide (TAA) was added and stirred for 30 min. Then the solution was transferred to a Teflon-lined autoclave and heated for 1, 5, 10, and 15 h at 100 °C. After cooling, the black products were centrifuged and washed with ethanol. Then, the products were dried overnight in an oven at 60 °C, and named as MCS-1, MCS-5, MCS-10 and MCS-15, respectively. The CS-5 and MS-5 were synthesized with the same process from Co-ZIF and Mn-ZIF.

Characterization

The crystal structure and surface morphology of products were examined by X-ray diffractometer (XRD, Smartlab SE), field emission scanning electron microscopy (FESEM, Zeiss, Gemini Sigma 300/VP) and transmission electron microscopy (TEM, FEI Talos F200X). The elemental composition was investigated by X-ray photoelectron spectroscopy (XPS, ESCALAB 250Xi). The specific surface areas and pore distribution of the samples were characterized by using a V-Sorb 2800 P nitrogen desorption/absorption instrument. The samples were also characterized by Fourier transform infrared spectroscopy (FTIR, Bruker Equinox 55).

Electrochemical measurements

In order to assess the electrochemical performance of hollow MCS nanospheres, a three-electrode measurement was conducted in 2 M KOH solution with a Pt foil and an Hg/HgO electrode as the counter and reference electrode. The sample's working electrode were prepared using the general "slurry" method and the average load mass was about 2 mg cm^{-2} on the Ni foam. The cyclic voltammetry (CV), galvanostatic charge/discharge (GCD) and electrochemical impedance spectroscopy (EIS) tests were performed on a CHI 660E electrochemical work station. The EIS measurements were performed at a frequency ranging from 10^{-2}–10^5 Hz with an AC amplitude of 5 mV. The cycling performance tests were performed on a CT2001A LAND battery test system.

An ASC was fabricated using the MCS-5 and activated carbon as positive and negative electrodes. A cellulose paper was used as a separator and 2 M KOH solution as electrolyte. The specific capacitance of the ASC was calculated according to the total mass of the active substances on the two electrodes. The optimized mass ratio of the positive electrode material to the negative electrode material was determined to be 0.5 according to the charge balance theory. Specific capacitance, specific energy, specific power calculation formulas are provided in ESI.†

Results and discussion

Materials characterization

The synthesis of hollow MCS nanospheres is illustrated in Scheme 1. The dual-ZIF precursor were firstly synthesized *via* precipitation reaction of Mn, Co metal ions and 2-MIM at room temperature. Then, the ion reassembling and sulfuration process coincided during the subsequently solvothermal treatment with TAA, transforming the dual-ZIF nanocrystals into hollow MCS nanospheres. The SEM images of the Mn, Co-ZIF are shown in Fig. 1a. The Mn, Co-ZIF displays regular

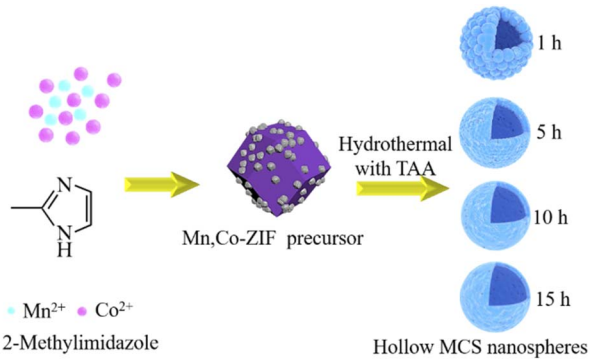

Scheme 1 Illustration of the synthesis process of MCS.

rhombic dodecahedral with a uniform diameter of about 400–600 nm and some small particles can be detected on the surface, corresponding to a mixture of Mn-ZIF and Co-ZIF. The SEM images of Mn-ZIF and Co-ZIF were shown in Fig. 1b and c. The reaction of 2 MIM ligands with Mn^{2+} and Co^{2+} ions results in a mixture of homometallic ZIFs rather than bimetallic ZIFs, which was in accord with previous reports.[28] The XRD measurements were also conducted to confirm the existence of the two ZIFs in Fig. 1d. It can be seen that the diffraction peaks in the Mn, Co-ZIF curves belong to two different phases of Mn-ZIF and Co-ZIF. The XRD patterns of the prepared Mn-ZIF and Co-ZIF are also shown in Fig. 1b, and the diffraction peaks of Co-ZIF correspond to the simulated ZIF-67 phase.

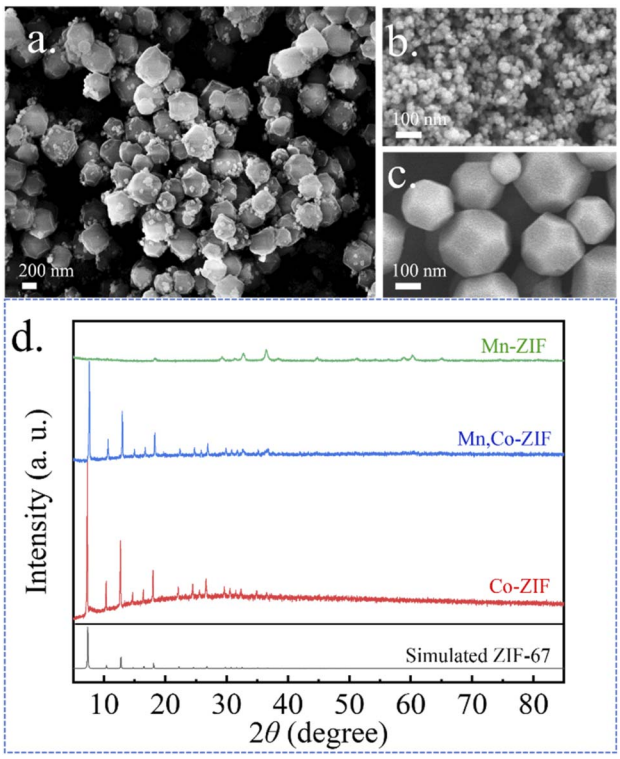

Fig. 1 SEM images of the (a) Mn, Co-ZIF, (b) Mn-ZIF, (c) Co-ZIF precursor and (d) XRD patterns.

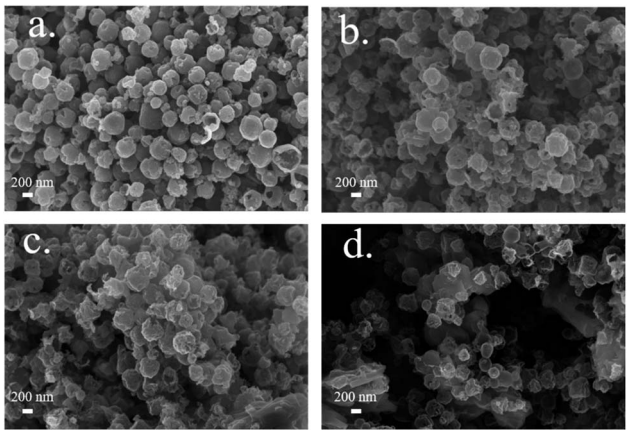

Fig. 2 SEM images of the (a) MCS-1, (b) MCS-5, (c) MCS-10 and (d) MCS-15.

The morphologies of the products were investigated by using FESEM (Fig. 2). After 1 h solvothermal reaction time, the solid precursors transformed into the hollow nanospheres with a rough surface, and the small particles began to disappear, implying the reassembling of the Mn-ZIF (Fig. 2a). After 5 h, small particles completely disappeared (Fig. 2b), and the spherical shell became thinner and rougher with the increasing reacting time. When 15 h, spheres began to collapse, resulting in ultra-thin nanoflakes (Fig. 2d). Meanwhile, the CS-5 and MS-5 were also synthesized. By contrast, CS-5 still maintained a hollow structure and MS-5 exhibited small particles (Fig. S1a and b†).

The phase transition during sulfuration of the MCS samples was studied by XRD measurements (Fig. 3a). It can be seen that the patterns exhibited very weak diffraction peaks, revealing the low crystallinity of the four samples. For MCS-1, the peaks at 10.42°, 12.78° and 18.10° can be attributed to the simulated ZIF-67 phase and the peaks at 32.30°, 36.23° can be attributed to the CoS_2 phase (JCPDS No. 41-1471), representing the occurring of the sulfuration reaction. The diffraction peaks disappeared when reacting from 5 h to 10 h and 15 h. It might be because the solvothermal process further reduces the crystalline degree of the MCS samples.[29,30] The XRD patterns of CS-5 and MS-5 were performed in Fig. S1c and d.† It can be seen that CS-5 displays low crystallinity without obvious diffraction peaks and the MS-5 curve shows the same diffraction peaks of Mn-ZIF. In order to confirm the functional groups, FTIR tests were performed and the results were shown in Fig. 3b. For the Mn, Co-ZIF, characteristic peaks at 2929 cm^{-1} and 3135 cm^{-1} are related to stretching and bending bonds of the C–H chain in the aliphatic methyl group and aromatic ring, the peak at 1448 cm^{-1} is attributed to stretching of the C=N bonds.[31,32] Furthermore, the peak at 425 cm^{-1} belongs to the Co–N bonds.[33] After sulfuration, there are 630 and 1095 cm^{-1}, corresponding to Co–S and Co=S in the spectrum, implying the successful sulfuration reaction.[34,35] The morphology and hollow interior structure of the MCS sample were further elucidated by TEM (Fig. 4). With the prolonged sulfuration time, unique hollow spheres were

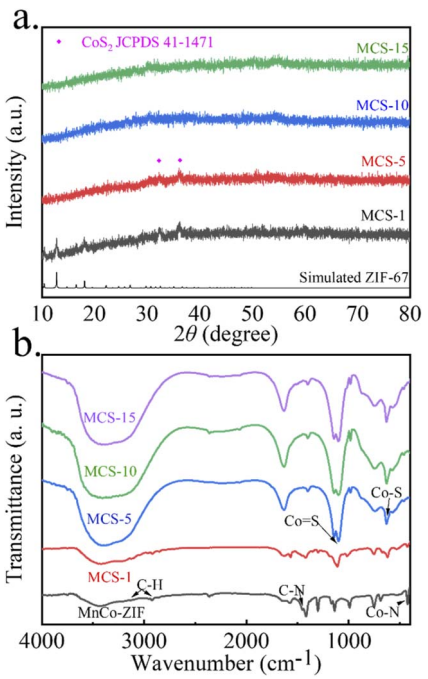

Fig. 3 (a) XRD patterns of the MCS-1, MCS-5, MCS-10 and MCS-15 and (b) FTIR spectrum of precursor, MCS-1, MCS-5, MCS-10 and MCS-15.

obtained. The pale center and dark edge of spheres confirm the existence of inner voids and the decreasing of the shell thickness (Fig. 4a–d). For the 1, 5, and 10 h reacting time, the shell thickness was about 40, 30 and 20 nm, separately (Fig. 4e–g). When reaction time reached 15 h, the thin shell collapsed as shown in Fig. 4d. Moreover, the energy dispersive spectrometer mapping (Fig. 4i–l) demonstrates the uniform distribution of Co and S elements in the MCS samples and the gradually uniform distribution of the Mn element. In Fig. 4i, the Mn element is mainly dispersed on the small particles, which should be the residual Mn-ZIF. When time surpasses 5 h (Fig. 4j–l), the Mn element tends to be uniform and disperse on the whole nanospheres, demonstrating a reassembling process. The intrinsic mechanism of the Mn-ZIF reassembling and hollow structure construction for the MCS samples might be due to the Kirkendall effect according to previous reports.[36] The intrinsic formation mechanism of hollow structure for the MCS samples are synthesized due to the Kirkendall effect. As the reaction proceeds, S^{2-} released from the decomposition of TAA react with metal ions on the surface of Co-ZIF. The solid cores are gradually consumed and the released metal ions diffuse to the outer shell to react with S^{2-}. Meanwhile, Mn^{2+} released from the decomposition of Mn-ZIF at reaction processed and incorporated in cobalt sulfide. As a result, manganese cobalt sulfide with hollow interior was formed. The nitrogen adsorption–

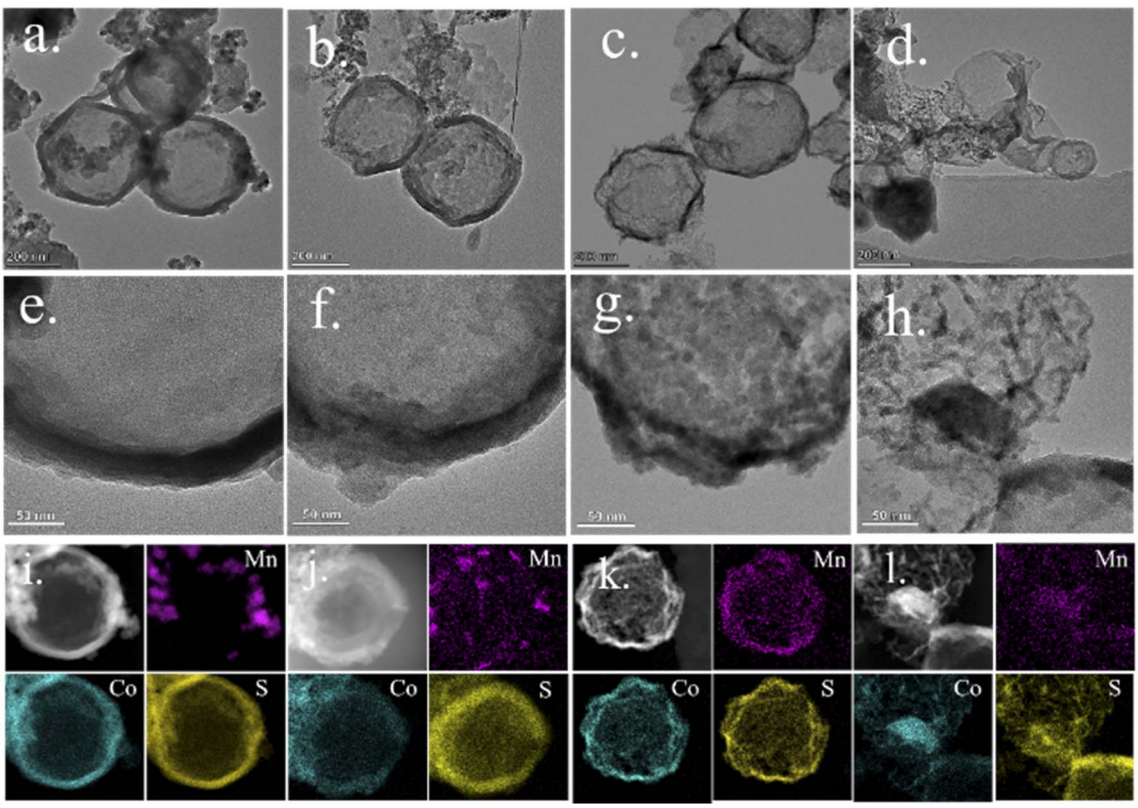

Fig. 4 TEM images of the (a and e) MCS-1, (b and f) MCS-5, (c and g) MCS-10, (e and h) MCS-15, and corresponding EDS mapping images for Mn, Co and S in the (i) MCS-1, (j) MCS-5, (k) MCS-10, (l) MCS-15.

Table 1 Specific surface areas, pore size distributions and pore volumes of the MCS samples

Sample	Surface area ($m^2\ g^{-1}$)	Pore volume ($cc\ g^{-1}$)	Pore diameter (nm)
MCS-1	33.3	0.28	2.83
MCS-5	25.7	0.34	2.18
MCS-10	21.4	0.19	3.92
MCS-15	28.0	0.34	2.03

desorption measurements were conducted to study the specific surface area and pore size distribution (Table 1). All the isotherms (Fig. S2†) exhibit hysteresis loops in the range of 0.5–1.0P/P_0 and belong to typical type-IV curves, confirming the presence of mesoporous structures in the materials.[37,38] The specific surface areas of MCS-1, 5, 10 and 15 are separately 33.3, 25.7, 21.4 and 28.0 $m^2\ g^{-1}$.

X-ray photoelectron spectroscopy (XPS) is used to further verify the chemical state of the MCS-5 as shown in Fig. 5a, exhibiting the existence of Co, Mn, S, C, N and O elements. For Co 2p spectrum (Fig. 5b), the peaks centered at around 778.3 eV and 793.4 eV can be assigned to of Co $2p_{3/2}$ and Co $2p_{1/2}$ spin–orbit.[18,39,40] For Mn 2p in Fig. 5c, the peaks centered at around 638.3 eV and 650.1 eV can be assigned to Mn $2p_{3/2}$ and Mn $2p_{1/2}$, which matches the standard spin–orbit.[41] The S 2p spectrum at 161.5 eV is ascribed to S $2p_{3/2}$ of cobalt sulfide binds (Fig. 5d). Other peaks at 162.6 eV correspond to S $2p_{1/2}$ of manganese sulfide bonds. Additionally, the peak at 168.7 eV was indexed to surface sulfur with partial oxidation of residual sulfide groups.[42,43]

Electrochemical performance of the MCS electrodes

In order to assess the electrochemical performance of the MCS samples, CV tests were performed as shown in Fig. 6a. All enclosed CV curves display obvious oxidization and reduction current peaks, suggesting a reversible faradaic reaction on the electrode. Significantly, the maximum integral area of MCS-5 than other electrodes implies its highest specific capacity.[44] Fig. 6b presents the GCD curves of the MCS samples at a current density of 1 A g^{-1}. The voltage plateaus of the GCD curves indicates the process of faradaic redox reactions, which is agreement with the CV results. Among them, the MCS-5 displayed the longest discharge time. The specific capacitance of MCS-1 ~ 15 can be calculated as 820.8, 957, 753.6 and 669 C g^{-1}. The GCD tests at other current densities were also conducted and the corresponding specific capacitances were shown in

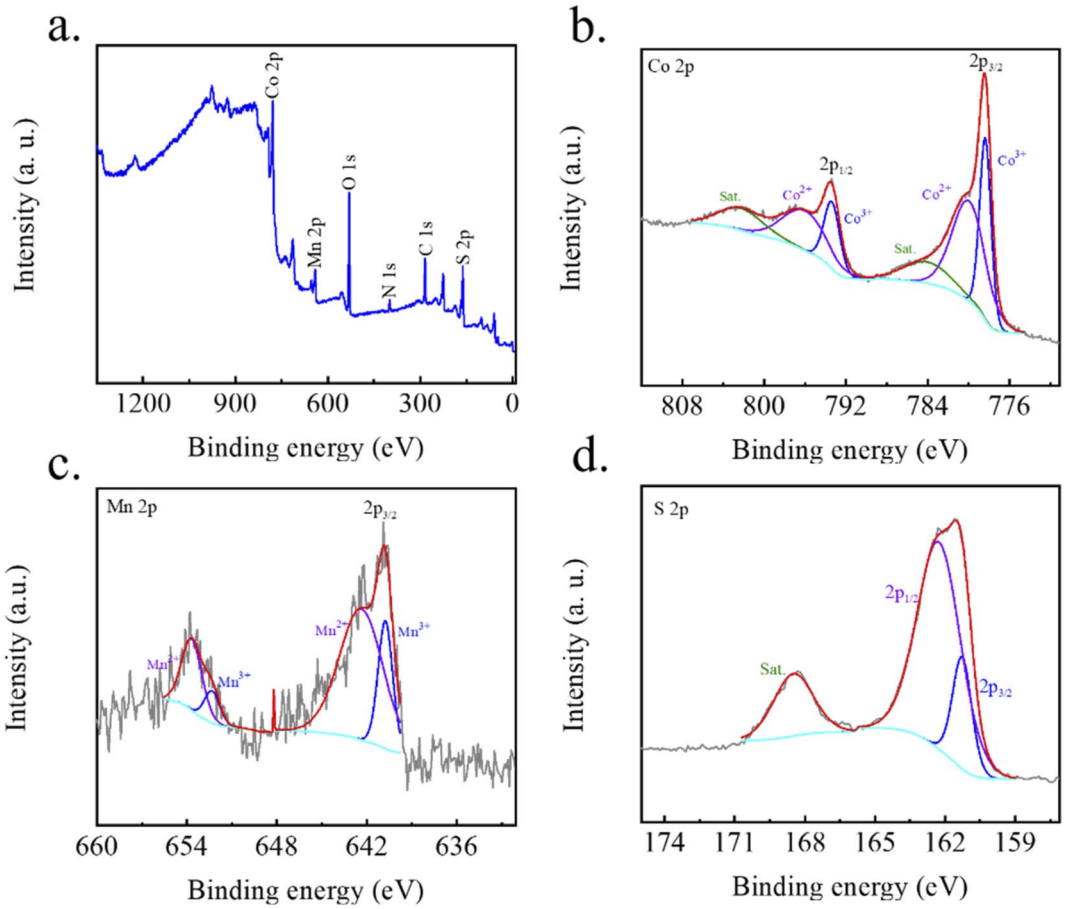

Fig. 5 (a) XPS spectra and high-resolution scan of the (b) Co 2p, (c) Mn 2p, (d) S 2p of the MCS-5. (e) N_2 adsorption–desorption isotherms, (f) Barrett–Joyner–Halenda desorption size–distribution plots of MCS samples.

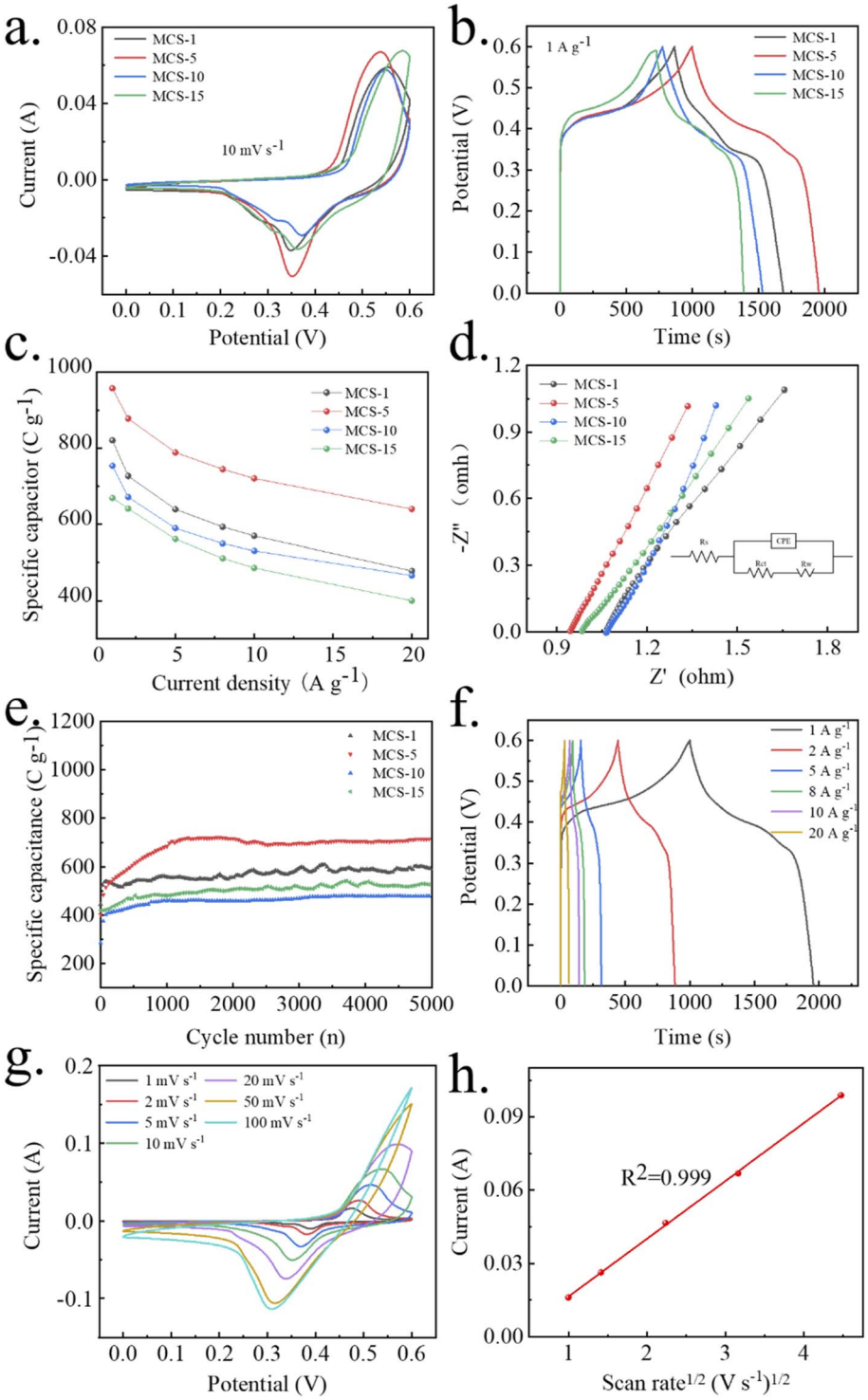

Fig. 6 Electrochemical properties of MCS electrodes (a) CV curves at 10 mV s^{-1}, (b) GCD curves at 1 A g^{-1}, (c) specific capacitance at different current densities, (d) Nyquist plots (the inset shows the stimulated diagram of equivalent circuit), (e) cycling stability at a constant current density of 5 A g^{-1}, (f) GCD curves of MCS-5 at different current densities, (g) CV curves of MCS-5 at different scan rates, and (h) the fitting result of current peak *vs.* scan rate$^{1/2}$.

Fig. 6c. The EIS measurement results were shown in Fig. 6d. The intersection with the *x*-axis at the high-frequency region reflects the resistance to the electrolyte (R_s), while the semicircle diameter denotes the charge transfer resistance (R_{ct}). Additionally, the straight line in the low-frequency region illustrates the diffusion resistance of electrolyte ions and carriers with hierarchical electrode material. The MCS-5 electrode displays a smallest R_{ct} value (0.83 Ω) than the others, MCS-

1 (1.447 Ω), MCS-10 (1.25 Ω) and MCS-15 (1.01 Ω), indicating the smallest contact resistance of the developed electrode. Interestingly, considering the reduction of R_{ct} from MCS-5 to other composites. In addition, the bulk solution resistances of the all composite are 1.07, 0.76, 0.77 and 0.83 Ω, respectively. The relatively larger slope of low frequency lines for the MCS-5 electrode, manifesting a lower ions diffusion resistance and thereby a higher energy storage behavior. The cycling performances of MCS electrodes were evaluated at current density of 5 A g^{-1} for 5000 cycles (Fig. 6e). There is no significant capacity decay, indicating the stability of MCS-5 during long-term cycling. With the activation process, more nanoparticles join the electrochemical process, offering higher specific capacitance.

As MCS-5 revealed the highest specific capacitance, the GCD curves of the MCS-5 electrode were tested at different current densities from 1 to 20 A g^{-1} (Fig. 6f). The discharge specific capacities are estimated to be 957, 877.8, 789, 744.6, 720.6 and 639.6 C g^{-1} at the current densities of 1, 2, 5, 8, 10 and 20 A g^{-1}, respectively. These values are superior to the electrochemical performance of CS-5 (694.8 C g^{-1} at 1 A g^{-1}) and MS-5 (456.6 C g^{-1} at 1 A g^{-1}) at the same condition (shown in Fig. S3†),

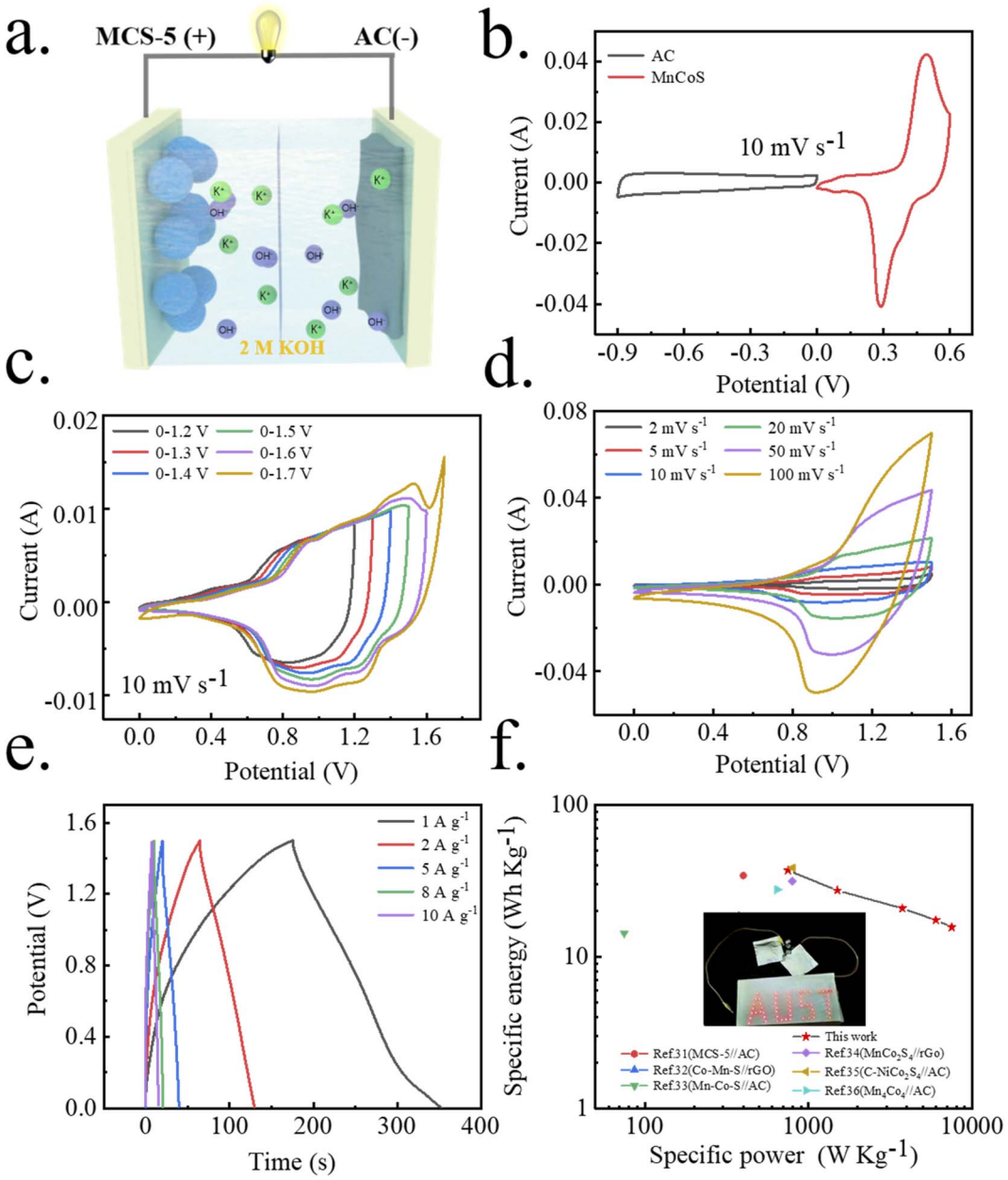

Fig. 7 (a) The schematic illustration of the assembled asymmetric supercapacitor, (b) CV curves of AC and MCS-5 electrodes at scan rate of 10 mV s^{-1}, (c) CV curves of the asymmetric device within different voltage range at scan rate of 10 mV s^{-1}, (d) GCD curves of the ASC device at different current densities, (e) CV curves of the ASC device at different scan rates, (f) the Ragone plot of the MCS-5//AC-ASC device (the inset shows light up LEDs).

implying the synergistic effect of manganese cobalt bimetallic sulfides. Furthermore, the CV measurement was tested under different potential scan rates (Fig. 7g and S4†). All CV profiles of MCS electrode materials have one pair of redox peaks. Limited by the ion diffusion rates, fewer ions participated in the reaction at the interface when the scan rate increased, resulting in the shifting position of oxidation and reduction current peaks towards the scanning directions. To further evaluate the charge storage mechanism of the MCS-5 electrode, the oxidization current peak values and corresponding scan rate$^{1/2}$ were linearly fitted in Fig. 7h. The square deviation R^2 is 0.999, revealing a controlled redox intercalation process.[45]

An ASC device was fabricated by using the capacitance type (active carbon, AC) and battery type (MCS-5) electrode as the cathode and anode (Fig. 7a). CV curves of the AC and MCS-5 electrode at 10 mV s^{-1} were displayed in Fig. 7b, which is a quasi-rectangular shape of a typical capacitive behavior with the potential window from −0.9 to 0 V and a pair of redox peaks with the potential window from 0 to 0.6 V. According to the charge balance formula ($Q^+ = Q^-$), the optimized mass ratio of the MCS-5//AC was measured to be 0.5. The final operating potential window of the MCS-5//AC is determined from 0 to 1.5 V due to the polarization phenomenon at 1.6 V (Fig. 7c). Moreover, the CV curves of MCS-5//AC almost maintain a pair of redox peaks at different potential scan rates (Fig. 7d), manifesting excellent faradaic redox reversible electrochemical. The GCD curves tested at different current densities are illustrated (Fig. 7e), where the inclined platform is considered as a combination of double-layer capacitance and faradaic capacitance behavior. The corresponding discharge time is estimated to be 177.1, 130.6, 99.5, 83.2 and 75 C g^{-1} at the current density of 1, 2, 5, 8 and 10 A g^{-1}, respectively.

Additionally, the specific energy and power of the MCS-5//AC device are also calculated. As shown in the Ragone plot (Fig. 7f), the MCS-5//AC device can deliver specific energy of 36.9, 27.2, 20.7, 17.3, and 15.6 W h kg^{-1} at specific power of 750, 1500, 3750, 6000 and 7500 W kg^{-1}, respectively. The Ragone plot indicates that the ASC devices, including. The comparison with previous reports indicates that the MCS-5//AC electrode is a promising candidate for use in high-performance supercapacitors.

Conclusions

In this work, a novel low-crystalline hollow MnCoS nanospheres (MCS) electrode material was synthesized through a "reassemble strategy" by a simple solvothermal synthesis for supercapacitors. The spherical shell surface structure, thickness and chemical composition were controlled *via* regulating the solvothermal reaction time. The electrochemical performances were systematically estimated. As the unique low-crystalline and optimized hollow nanosphere structures contribute to increasing active sites, MCS exhibits excellent electrochemical performance. The test results show that the specific capacitance increases with increasing solvothermal time, and the MCS with 5 h reacting time exhibits optimal electrochemical properties with a high specific capacity of 957 C g^{-1} (1 A g^{-1}). Furthermore, an MCS-5//AC asymmetric supercapacitor device delivers an specific energy as high as 36.9 W h kg^{-1} at a specific power of 750 W kg^{-1}.

Author contributions

Song Liu and Kun Chen: investigation. Song Liu: writing. Kun Chen: original draft. Jianjun Li and Jinbo Zhu: formal analysis and resources. Changguo Xue and Shibin Nie: writing-review & editing and supervision.

Conflicts of interest

There are no conflicts to declare.

Acknowledgements

This work was supported by the Talent Research Start-up Fund of Anhui University of Science and Technology, National Natural Science Foundation of China (Grant No. 11872001 and 12172002), the Key Research and Development Program Projects in Anhui Province 2020 (Grant No. 202004h07020026), the University Synergy innovation Program of Anhui Province (Grant No. GXXT-2022-018).

Notes and references

1 J.-H. Cao, Y.-Z. Hu, Y.-Y. Zhu, H. Cao, M.-Q. Fan, C.-H. Huang, K.-Y. Shu, M.-X. He and H.-C. Chen, *Chem. Eng. J.*, 2021, **405**, 126928.
2 S. Jin, H. Lee and S. Yim, *RSC Adv.*, 2019, **9**, 31846.
3 M.-B. Askari, P. Salarizadeh, M. Seifi, S.-M. Rozati and A. Beheshti-Marnani, *Nanotechnology*, 2020, **31**, 275406.
4 Z.-Y. Song, L. Miao, L.-C. Li, D.-Z. Zhu, L.-H. Gan and M.-X. Liu, *Carbon*, 2021, **180**, 135.
5 H. Liu, Z. Li, Z. Yao, Y. Liu, Q. Zhang, Y. Sun and Z. Li, *J. Colloid Interface Sci.*, 2019, **551**, 119.
6 Y. Zhou, Z.-X. Jia, S.-Y. Zhao, P. Chen, Y.-N. Wang, T. Guo, L.-Y. Wei, X.-M. Cui, X.-P. Ouyang, X. Wang, J.-W. Zhu, J.-W. Sun, S.-G. Pan and Y.-S. Fu, *Chem. Eng. J.*, 2021, **416**, 129500.
7 Q.-Q. Qin, D.-W. Ou, C.-J. Ye, L.-X. Chen, B.-B. Lan, J. Yan and Y.-C. Wu, *Electrochim. Acta*, 2019, **305**, 403.
8 C. V. V. M. Gopi, R. Vinodh, S. Sambasivam, I. M. Obaidat, S. Singh and H. J. Kim, *Chem. Eng. J.*, 2020, **381**, 122640.
9 X.-L. Wang, J. Gao, X.-X. Wu, R.-H. Que and K.-L. Wu, *RSC Adv.*, 2016, **6**, 54142.
10 C.-Z. Wie, Y.-T. Sun, N.-N. Zhan, M.-Y. Liu, L.-Y. Zhao, C. Cheng and D.-J. Zhang, *ChemistrySelect*, 2017, **2**, 11154.
11 A.-M. Elshahawy, X. Li, H. Zhang, Y.-T. Hu, K.-H. Ho, C. Guan and J. Wang, *J. Mater. Chem. A*, 2017, **5**, 7494.
12 X.-Z. Song, F.-F. Sun, Y.-L. Meng, Z.-W. Wang, Q.-F. Su and Z. Tan, *New J. Chem.*, 2019, **43**, 3601.
13 T. Huang, X.-Z. Song, X. Chen, X.-L. Chen, F.-F. Sun, Q.-F. Su, L.-D. Li and Z. Tan, *New J. Chem.*, 2018, **42**, 5128.
14 L. Wang, Y.-F. Yuan, X.-T. Zhang, Q. Chen and S.-Y. Guo, *Nanotechnology*, 2019, **30**, 355401.

15 H. Duan, Z.-Y. Song, L. Miao, L.-C. Li, D.-Z. Zhu, L.-H. Gan and M.-X. Liu, *J. Mater. Chem. A*, 2022, **10**, 9837.
16 F.-F. Zhang, M. Cho, T. Eom, C. Kang and H. Lee, *Ceram. Int.*, 2019, **45**, 20972.
17 G. Li, Z.-Q. Chang, T.-Y. Li, L.-L. Ma and K.-Y. Wang, *Ionics*, 2019, **25**, 3885.
18 L.-F. Shen, L. Yu, H.-B. Wu, X.-Y. Yu, X.-G. Zhang and X.-W. Lou, *Nat. Commun.*, 2015, **6**, 6694.
19 S.-J. Peng, L.-L. Li, H.-T. Tan, R. Cai, W.-H. Shi, C.-C. Li, S.-G. Mhaisalkar, M. Srinivasan, S. Ramakrishna and Q.-Y. Yan, *Adv. Funct. Mater.*, 2014, **24**, 2155.
20 T.-J. Qiu, S. Gao, Z.-B. Liang, D.-G. Wang, H. Tabassum, R.-Q. Zhong and R.-Q. Zou, *Angew. Chem., Int. Ed.*, 2021, **60**, 17314.
21 S. Sanati, R. Abazari, J. Albero, A. Morsali, H. García, Z.-B. Liang and R.-Q. Zou, *Angew. Chem., Int. Ed.*, 2021, **60**, 11048.
22 Y. Huang, Y. Fang, X.-F. Lu, D. Luan and X.-W. Lou, *Angew. Chem., Int. Ed.*, 2020, **59**, 19914–19918.
23 J.-C. Zhang, L.-H. Liu, G. Qian, Z.-J. Zhou, K.-S. Xiao, S. Cheng, Y. Wang, Y.-F. Liu and Y. Feng, *New J. Chem.*, 2019, **43**, 2171.
24 Y. Huang, S.-L. Zhang, X.-F. Lu, Z.-P. Wu, D.-Y. Luan and X.-W. Lou, *Angew. Chem., Int. Ed.*, 2021, **60**, 11841.
25 J. Liu, C. Wu, D.-D. Xiao, P. Kopold, L. Gu, P. A. van Aken, J. Maier and Y. Yu, *Small*, 2016, **12**, 2354.
26 P. Zhang, B.-Y. Guan, L. Yu and X.-W. Lou, *Angew. Chem., Int. Ed.*, 2017, **56**, 7141.
27 J. Tang, R. R. Salunkhe, J. Liu, N. L. Torad, M. Imura, S. Furukawa and Y. Yamauchi, *J. Am. Chem. Soc.*, 2015, **137**, 1572.
28 J. Pan, S.-B. Li, F.-B. Li, T.-T. Yu, Y.-P. Liu, L. Zhang, L. Ma, M. Sun and X.-F. Tian, *Colloids Surf., A*, 2021, **609**, 125650.
29 Y.-Y. Dong, Y. Wang, Y.-A. Xu, C.-C. Chen, Y.-J. Wang, L.-F. Jiao and H.-T. Yuan, *Electrochim. Acta*, 2017, **225**, 39.
30 R.-S. Gao, Q.-G. Zhang, F. Soyekwo, C.-X. Lin, R.-X. Lv, Y. Qu, M.-M. Chen, A.-M. Zhu and Q.-L. Liu, *Electrochim. Acta*, 2017, **237**, 94.
31 Y. Zhao, Z. Shi, H. Li and C.-A. Wang, *J. Mater. Chem. A*, 2018, **6**, 12782.
32 A. Khan, M. Ali, A. Ilyas, P. Naik, I. F. J. Vankelecom, M. A. Gilani, M. R. Bilad, Z. Sajjad and A. L. Khan, *Sep. Purif. Technol.*, 2018, **206**, 50.
33 T. Truong, T. M. Hoang, C. K. Nguyen, Q. T. N. Huynh and N. T. S. Phan, *RSC Adv.*, 2015, **5**, 24769–24776.
34 X.-Y. Li, X.-Y. Gao, L.-H. Ai and J. Jiang, *Chem. Eng. J.*, 2015, **274**, 238.
35 M. Jin, S.-Y. Lu, L. Ma, M.-Y. Gan, Y. Lei, X.-L. Zhang, G. Fu, P.-S. Yang and M.-F. Yan, *J. Power Sources*, 2017, **341**, 294.
36 L. Zhang, H.-B. Wu and X.-W. Lou, *Chem. Commun.*, 2012, **48**, 6912.
37 W. Wang, M. Dahl and Y. Yin, *Chem. Mater.*, 2012, **25**, 1179.
38 S. Kandula, K.-R. Shrestha and N.-H. Lee, *Small*, 2018, **14**, 1800291.
39 R. Miao, J. He, S. Sahoo, Z. Lou, W. Zhong, S.-Y. Chen, C. Guild, T. Jafari, B. Dutta, S.-A. Cetegen, M. Wang, S.-P. Alpay and S.-L. Suib, *ACS Catal.*, 2016, **7**, 819.
40 H. Wan, X. Ji, J. Jiang, J. Yu, L. Miao, L. Zhang, S. Bie, H. Chen and Y. Ruan, *J. Power Sources*, 2013, **243**, 396.
41 Z. Yang, C.-Y. Chen and H.-T. Chang, *J. Power Sources*, 2011, **196**, 7874.
42 R. B. Pujari, A. C. Lokhande, A. A. Yadav, J. H. Kim and C. D. Lokhande, *Mater. Des.*, 2016, **108**, 510.
43 Y.-Y. Zhu, H.-C. Chen, S. Chen, C. Li, M.-Q. Fan and K.-Y. Shu, *J. Mater. Sci.*, 2018, **53**, 6157.
44 K.-Y. Zhang, Y.-H. Wei, J. Huang, Y.-B. Xiao, W.-Z. Yang, T. Hu, K. Yuan and Y.-W. Chen, *Sci. China Mater.*, 2020, **63**, 1898.
45 X. Yu, M.-Y. Wang, A. Gagnoud, Y. Fautrelle, R. Moreau and X. Li, *Electrochim. Acta*, 2017, **248**, 150.